Proc. Natl. Acad. Sci. USA
Vol. 92, pp. 10277–10281, October 1995
Biophysics

Crystal structure of the I-domain from the CD11a/CD18 (LFA-1, $\alpha_L\beta 2$) integrin

(metal-binding site/protein structure/cell–cell adhesion/von Willebrand disease)

AIDONG QU AND DANIEL J. LEAHY*

Department of Biophysics and Biophysical Chemistry, Johns Hopkins University School of Medicine, 725 North Wolfe Street, Baltimore, MD 21205

Communicated by Thomas D. Pollard, Johns Hopkins University School of Medicine, Baltimore, MD, July 5, 1995

ABSTRACT **We report the 1.8-Å crystal structure of the CD11a I-domain with bound manganese ion. The CD11a I-domain contains binding sites for intercellular adhesion molecules 1 and 3 and can exist in both low- and high-affinity states. The metal-bound form reported here is likely to represent a high-affinity state. The CD11a I-domain structure reveals a strained hydrophobic ridge adjacent to the bound metal ion that may serve as a ligand-binding surface and is likely to rearrange in the absence of bound metal ion. The CD11a I-domain is homologous to domains found in von Willebrand factor, and mapping of mutations found in types 2a and 2b von Willebrand disease onto this structure allows consideration of the molecular basis of these forms of the disease.**

CD11a/CD18 (LFA-1, $\alpha_L\beta 2$) is a member of the integrin family of cell surface receptors. Integrins consist of a 120- to 180-kDa α subunit (CD11a in this case) and a 90- to 110-kDa β subunit (CD18 or $\beta 2$ in this case) that are noncovalently associated single-pass transmembrane proteins. The bulk of each integrin subunit is extracellular, where it typically functions as a receptor for extracellular matrix molecules or counterreceptors on the surface of apposed cells (1). CD11a/CD18 is expressed on all leukocytes and mediates adhesion to a variety of cell types that express one or more of the CD11a/CD18 ligands intercellular adhesion molecule 1 (ICAM-1), ICAM-2, and ICAM-3. The processes mediated by CD11a/CD18 interactions include adhesion to the endothelium and extravasation at sites of inflammation and adherence of activated T cells to target cells (2). A subset of integrin α chains, including CD11a, contain an inserted domain (I-domain) of ≈190 aa that is homologous to the family of von Willebrand Factor (vWF) A-type domains (3, 4). The I-domain has been associated with ligand binding in each of the I-domain-containing integrins (5–11).

Many integrins do not normally exhibit high affinity for ligands and must become activated for an interaction with ligand to be observed (1, 12, 13). The conversion to a high-affinity state is typically transiently induced after appropriate physiological stimuli to the integrin-bearing cell. The production of monoclonal antibodies that specifically recognize the active state of integrins and the observation of altered biophysical properties following ligand binding have led to the belief that a conformational change accompanies the transition to the high-affinity state in integrins (1). The mapping of both ligand-binding and active-state antibody epitopes to the I-domains of I-domain-containing integrins indicates that any activation-dependent conformational change is likely to involve the I-domain (7, 8, 14). The presence of a conserved divalent cation-binding site in I-domains and the requirement of divalent cations for ligand binding indicate that the metal-bound form of the I-domain is likely to represent a high-affinity state (6, 15). A regulated affinity for ligand is also observed for the interaction between the vWF A domains and the platelet receptor GPIb (16), suggesting that conformational regulation of affinity for ligand may be a general feature of this type of domain.

We undertook an x-ray crystallographic study of the CD11a I-domain to investigate the structural features of affinity modulation and ligand binding in this domain and to provide a basis for modeling homologous domains in other proteins. Recently, the crystal structure of the I-domain from CD11b with bound magnesium was reported (17). The CD11b I-domain amino acid sequence matches the CD11a sequence at 33% of the positions, and the CD11b structure showed these domains to possess a flavodoxin-like tertiary structure and allowed identification of a set of conserved residues involved in coordinating the metal ion. We report here the refined 1.8-Å crystal structure of the CD11a I-domain with bound manganese ion.† A strained hydrophobic ridge adjacent to the bound metal ion is seen that may be involved in ligand binding and that is likely to undergo rearrangement in the absence of bound metal. We have also mapped von Willebrand disease (vWD)-causing mutations found in vWF A domains onto the CD11a I-domain structure and consider molecular mechanisms that may underlie different forms of vWD.

MATERIALS AND METHODS

Expression and Purification of the CD11a I-Domain. A DNA fragment encoding residues Cys-125 to Gly-311 of human CD11a (CD11a-I) was amplified by reverse transcription–PCR from the monocytic cell line THP-1 (18). The DNA sequence of this fragment was determined and was found to agree with published sequences (3) with the exception of a T → C mutation that results in an Arg at position 189 instead of a Trp. Since multiple independent inserts contained this mutation and the proofreading *Pfu* polymerase was used, this mutation may represent an isoform. The CD11a gene fragment was subcloned into the pET11c expression vector and transformed into *Escherichia coli* BL21(DE3) and 834(DE3) cells (19). Three to 4 hr after induction of logarithmic-phase cells with isopropyl β-D-thiogalactopyranoside, the cells were harvested and lysed by sonication. The CD11a-I protein was found in the insoluble fraction of the lysate and resolubilized in 7 M urea/5 mM $MnCl_2$/10 mM Tris, pH 7.5/40 mM 2-mercaptoethanol. The resolubilized pellet was dialyzed in successive steps over 2 days into 5 mM $MnCl_2$/10 mM Tris, pH 7.5/5 mM 2-mercaptoethanol. A precipitate was removed by centrifugation, and the supernatant was concentrated by ultrafiltration and loaded onto a Pharmacia Mono-Q column. The CD11a-I

The publication costs of this article were defrayed in part by page charge payment. This article must therefore be hereby marked "*advertisement*" in accordance with 18 U.S.C. §1734 solely to indicate this fact.

Abbreviations: ICAM, intercellular adhesion molecule; vWF, von Willebrand factor; vWD, von Willebrand disease; SeMet, selenomethionyl-substituted; MAD, multiwavelength anomalous diffraction.

*To whom reprint requests should be addressed.

†The atomic coordinates and structure factors have been deposited in the Protein Data Bank, Chemistry Department, Brookhaven National Laboratory, Upton, NY 11973 (reference 1LFA, 1LFA-SF).

protein passed through the column and was judged ≥98% pure on a Coomassie-blue-stained SDS/polyacrylamide gel following concentration by vacuum dialysis in a collodion bag (Schleicher & Schuell). Selenomethionyl-substituted (SeMet) protein was prepared by using the methionine-auxotrophic strain 834(DE3) as described (20) and was purified in the same manner as the native protein.

Crystallization. Crystals were grown from hanging drops by the method of vapor diffusion. One microliter of 5 mM $MnCl_2$/5 mM 2-mercaptoethanol containing CD11a-I at 15 mg/ml was mixed with 1 μl of a reservoir solution of 14–20% (wt/vol) PEG 3350/100 mM $MnCl_2$/50 mM sodium acetate, pH 5.2, and equilibrated over the reservoir solution. Microseeding proved useful for both native and SeMet protein. Diffraction-quality crystals of SeMet protein were obtained only when the crystallization trials were carried out with degassed buffers in an anaerobic chamber. Crystals typically grew to a final size of 0.2 mm × 0.1 mm × 0.1 mm over 3–7 days. Most crystals were in space group *C*2 with unit cell dimensions a = 131.13 Å, b = 45.45 Å, c = 66.13 Å, and β = 99.8°. The largest SeMet crystal was in space group *P*222 with unit cell dimensions a = 66.12 Å, b = 129.22 Å, and c = 45.46 Å. This crystal was used for multiwavelength anomalous diffraction (MAD) experiments.

Data Collection and Processing. All data were collected from crystals soaked for at least 15 min in reservoir buffer containing 20% (wt/vol) PEG and 10% (vol/vol) ethylene glycol and flash-frozen in a gaseous nitrogen stream at −180°C. Diffraction data were collected from native *C*2 and SeMet *P*222 crystal forms with an R-axis IIc detector and Cu Kα radiation from a Rigaku RU200 rotating anode. MAD data were collected from a single SeMet *P*222 crystal that was transported frozen to the X4A beamline of the National Synchrotron Light Source at Brookhaven National Laboratory. MAD data were collected with Fuji HR-5 phosphor imaging plates. Two-degree oscillations at ϕ and ϕ + 180° were collected with no overlap for each oscillation range at each wavelength. All diffraction images were processed with the program DENZO and scaled with the program SCALEPACK (21). $\langle I+\rangle$ and $\langle I-\rangle$ were used for MAD phase determination, and partially recorded reflections were used in all cases. Diffraction data from different wavelengths were scaled with WVLSCL, and F_A values and optimal f' and f'' values were calculated with MADLSQ (22).

Structure Determination. Four selenium sites were deduced from inspection of F_A Patterson and difference Fourier maps, and these sites were confirmed with the program HEAVY. Phase determinations were made with the program MLPHARE, and solvent flattening and histogram matching were performed with the program DM (23). A complete atomic model for residues Asn-129 to Tyr-307 was readily built into 2.6-Å electron density maps by using the program O (24). The placement of this model in the unit cell indicated that the asymmetric unit must contain an additional molecule. All four selenium sites were accounted for by the first model, however, and no interpretable density existed for a second molecule. The initial model was thus used as a search model for molecular replacement with the *C*2 crystal form. Two solutions were found in the asymmetric unit of the *C*2 crystal form by use of X-PLOR (25), and all refinement was carried out in this crystal form. Several rounds of simulated annealing and/or Powell minimization with X-PLOR alternated with model building with O have produced the current atomic model for CD11a-I. This model consists of residues Gly-128 to Ile-309 for one molecule in the asymmetric unit, Gly-128 to Glu-310 for the other molecule (2941 nonhydrogen protein atoms), 2 manganese ions, 2 chloride ions, and 312 water molecules. A chloride ion has been modeled in one of the manganese coordination sites, as the distance to the manganese at this site (2.55 Å) is more compatible with chloride than with water, difference Fourier maps indicate a strong scatterer at this position, the charge on a chloride would neutralize the metal coordination sphere, and chloride is the only monoatomic anion added to the buffer. The rms difference in position for all main-chain atoms following superposition of the independent molecules in the asymmetric unit is 0.17 Å. Refinement statistics and stereochemical parameters for this model are shown in Tables 1–3.

RESULTS

The CD11a I-domain structure consists of a five-stranded parallel β-sheet core surrounded on both faces by α-helices (Fig. 1). A short antiparallel strand occurs on one edge of this sheet. The position of secondary structural elements in the CD11a sequence is shown in Fig. 2. This structure is very similar to that of flavodoxin (26) and members of the dinucleotide-binding family of proteins (27). The topology of the CD11a I-domain is essentially identical to that reported for the CD11b I-domain (17), with the exception that a 7-aa deletion between β-strands 3 and 4 (β3 and β4) in CD11a relative to CD11b results in the shortening of α-helix 5 (α5) to a single turn of 3_{10}-helix. Single turns of 3_{10}-helix are also found at the end of α6 (Leu-274 to Phe-277), between α4 and β3 (Arg-221 to Gly-225; not shown in Fig. 1), and between β4 and α6 (Lys-263 to Gln-266). An unusual turn is found between β2 and β2′ that contains a hydrogen bond from the amide of Ser-175 to the carbonyl of Ser-177. This turn appears similar to a γ turn, with the difference that the direction of the main-chain hydrogen bond is reversed. The only residues identified to be in highly strained regions of a Ramachandran plot by the program PROCHECK (28) are Ser-175, Leu-204, and Leu-205. Electron density for each of these residues is persuasive, and stabilizing hydrogen bonds exist in all cases.

The residues whose side chains coordinate the metal ion in the CD11a and CD11b I-domains are completely conserved [the so-called MIDAS motif (17)], but the manner in which the metal is coordinated differs slightly. As shown in Fig. 3 for the CD11a I-domain, the side chains of Ser-139, Ser-141, and Asp-239 directly coordinate the bound metal while the side chains of Thr-206 and Asp-137 are hydrogen-bonded to coordinating water molecules. In the CD11b I-domain the Thr-206 homologue directly coordinates the metal while the Asp-239 equivalent is hydrogen-bonded to a coordinated water molecule. Comparison of the CD11a I-domain structure with the published figures of the CD11b I-domain suggests that these differences in coordination may be achieved by a rotation of the coordinated metal ion. Other than affecting the interactions with Thr-206 and Asp-239, the principal effects of such a rotation would be to alter the orientation of the most solvent-exposed metal coordination position. The differences in metal coordination seen in the CD11a and CD11b structures may thus reflect a difference between I-domains with protein-liganded and solvent-exposed metal-binding sites. There seems little reason to believe any significant structural or functional differences exist between Mn^{2+}- and Mg^{2+}-bound forms of I-domains, and any variations in the physiological effects of these ions seems likely to be due to their differing affinities for I-domains (15).

Another notable difference between the CD11a and CD11b I-domain structures appears to be the disposition of α7 relative to the body of the I-domain. The extent of α7 is identical in CD11a and CD11b, and comparison of the α7 sequences in the two molecules reveals identical residues at 50% of the positions and residues conserved in type at >90% of the positions. Despite these similarities, α7 appears to have undergone significant rigid-body motion when the structure of the CD11a and CD11b I-domains are compared. A likely source for this motion is found by examination of intermolecular contacts for CD11a. α7 forms the C terminus of I-domains, and the C termini of the two CD11a I-domains in the asymmetric unit of

Table 1. MAD structure-factor ratios and anomalous scattering factors

	Structure-factor ratio*				Anom.†	
λ, Å	0.9871	0.9793	0.9790	0.9686	$f'(e)$	$f''(e)$
0.9871	0.032	0.045	0.034	0.032	−4.03	0.51
0.9793		0.047	0.032	0.049	−9.77	3.95
0.9791			0.058	0.037	−7.09	5.55
0.9686				0.048	−3.59	4.00

*Ratio = (rms ($\Delta|F|$))/(rms ($|F|$)), where ΔF is the Bijvoet difference at one wavelength (diagonal elements) or the dispersive difference between two wavelengths (off-diagonal elements). Centric data were merged to a single value and are thus not shown. The Bijvoet difference at λ1 may be taken instead as an upper limit of the noise of the anomalous signals.

†Anomalous components of the selenium scattering factors as a function of wavelength as determined by MADLSQ (22).

Table 2. Data collection statistics

Crystal	λ, Å	Resolution, Å	No. of reflections	Completeness, %	R_{sym}	$\langle I/\sigma I\rangle$
*P*222	0.9871	30–2.6	10,170	80.5	6.3	19.1
*P*222	0.9793	30–2.6	10,207	80.8	6.7	19.6
*P*222	0.9790	30–2.6	10,105	79.9	7.3	19.0
*P*222	0.9686	30–2.6	10,162	80.5	6.7	18.1
*C*2	1.54	30–2.1	21,810	95.5	3.8	21.6
*C*2	1.54	30–1.8	27,543	76.0	4.0	20.3

R_{sym} and completeness values were calculated by considering Bijvoet's equivalent. $R_{sym} = 100 \times \Sigma_h\Sigma_i|I_i(\mathbf{h}) - \langle I(\mathbf{h})\rangle|/\Sigma_h\Sigma_i I_i(\mathbf{h})$.

Table 3. Refinement and stereochemical statistics for *C*2 crystal form

R value	0.190 ($F > 2\sigma$, 6.0–1.8 Å), 0.193 (all *F*, 6.0–1.8 Å)
R free	0.251 ($F > 2\sigma$, 6.0–1.8 Å), 0.256 (all *F*, 6.0–1.8 Å)
rms deviation	
Bonds, Å	0.009
Angles	1.9°
B value	1.2 /1.3 (bonds/angles, main chain)
	2.3/2.7 (bonds/angles, side chain)
Avg. *B*, Å^2	14.9 (protein), 26.9 (solvent)

A subset of the data (5%) was excluded from refinement and used for the free *R*-value calculation (25). All data for which $|F| > 2\sigma$ were used in the refinement. *R* value = $\Sigma||F_o| - |F_c||/\Sigma|F_o|$.

the crystal structure reported here interact in such a way that residues 305–308 intercalate between α7 and the body of the molecule. As the CD11a I-domain is normally embedded in the much larger CD11a polypeptide, this interaction is almost certainly an artifact of crystal packing. α7 appears nonetheless quite labile, and this lability may prove a contributing factor to any conformational changes associated with the activation of CD11a/CD18 for ligand. A more complete consideration of structural differences between the CD11a and CD11b I-domains awaits direct comparison of atomic coordinates.

DISCUSSION

We have determined the high-resolution crystal structure of the I-domain of CD11a with bound manganese ion. The CD11a I-domain has been shown to contain a binding site for the CD11a/CD18 ligands ICAM-1 and ICAM-3 (7), but some manner of activation is required for this binding to be observed. This activation is believed to be accompanied by a conformational change in the integrin, most likely involving the I-domain. The ability of manganese ion to induce the active state and the requirement of divalent cations for ligand binding indicate that the manganese-bound form of the CD11a I-domain is likely to represent a high-affinity state of the molecule.

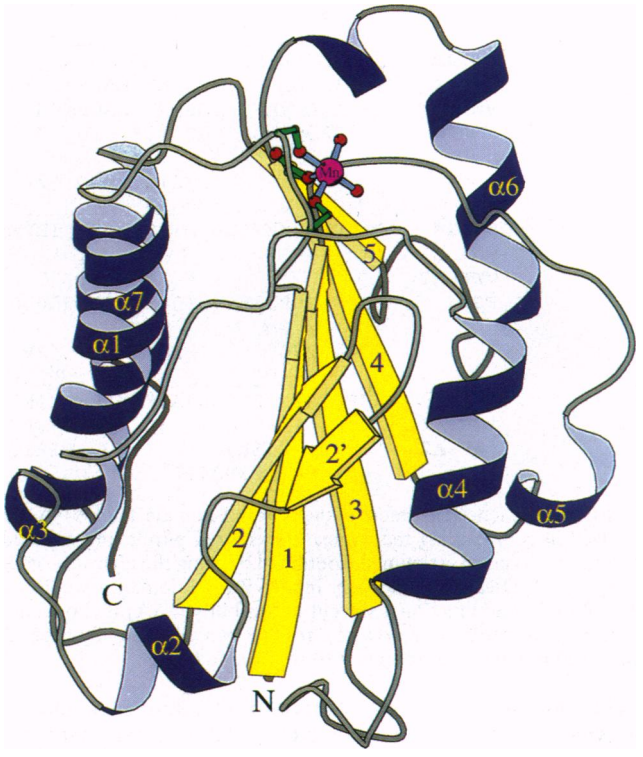

FIG. 1. Ribbon diagram of the CD11a I-domain. The manganese ion is shown in purple and the side chains of Ser-139, Ser-141, and Asp-239 are shown in green with red oxygen atoms. The N and C termini, the β-strands (yellow arrows), and the α-helical segments are labeled. This figure was made with the program MOLSCRIPT (26).

The presence in the CD11a I-domain structure of a strained hydrophobic ridge with main-chain contacts to the loop primarily responsible for coordinating the metal ion is consistent with both the existence of a conformational change upon activation and that the metal-bound state represents this active form. As shown in Fig. 3, Leu-203, Leu-204, Leu-205, and Met-140 form a solvent-exposed hydrophobic ridge adjacent to the metal-binding site. In addition to the energetic cost of exposing these hydrophobic residues, the main-chain torsion angles of Leu-204 ($\phi = -126$, $\psi = -138$) and Leu-205 ($\phi = -82$, $\psi = -159$) exist in highly unfavorable regions of ϕ, ψ space. These strained conformations are stabilized by the presence of the manganese ion through multiple main-chain hydrogen bonds between these residues and the metal-coordinating loop (residues 137–141). The presence of main-chain contacts between the hydrophobic ridge and the metal-coordinating loop suggests that this conformation is potentially independent of the amino acid sequence and may be a general feature of metal-bound states of I-domains. Metal coordination is also likely to affect the conformation of leucines 203–205 through their immediate successor in amino acid sequence, Thr-206, which forms hydrogen bonds with a metal-coordinated water in the CD11a structure and directly coordinates the metal in the CD11b structure (17). The conformation of the hydrophobic ridge is also stabilized through multiple hydrogen bonds to the unusual β-turn (residues 174–176) that contains the only other residue in the CD11a I-domain, Ser-174, with unfavorable main-chain torsion angles ($\phi = -155$, $\psi = -108$). Thus, two energetically strained loops exist whose conformations are stabilized directly and indirectly by the metal-coordinating loop. Significant rearrangements in these regions seem likely upon removal of the metal ion and may underlie the conformational change believed to occur during the transition between high- and low-affinity states of CD11a/CD18. The presence of this exposed hydrophobic

```
                130        140        150        160        170        180        190
                  . β1       .          α1         .          β2       β2'.  α2     .
CD11a     CIKGNVDLVFLFDGSMSLQPDEFQKILDFMKDVMKKLSNT--SYQFAAVQFSTSYKTEFDFSDYVKRKDP
vWF-A1    (513)LDLVFLLDGSSRLSEAEFEVLKAFVVDMMERLRISQKWVRVAVVEY      ··52aa··
vWF-A2    (734)LDVAFVLEGSDKIGEADFNRSKEFMEEVIQRMDVGQDSIHVTVLQY      ··54aa··
FSA         731000000000610685105300300120044138 3--42100000003715100103304663 40

                200        210        220        230        240        250        260
              α3   .       .  α4      .          .  β3      .          α5   β4  .
CD11a     DALLKHVKHMLLLTNTFGAINYVATEVFREELGARPDATKVLIIITDGEATDSGNIDAAKDIIRYIIGIG
vWF-A1                                          RPEASRIALLLMASQEP  ·18aa·  VIVIPVGIG
vWF-A2                                          REQAPNLVYMVTGNPAS  ·9aa·  IQVVPIGVG
FSA       5100570811564010020032005400366320157042000000014032976053056030300000

                270        280        290        300        310
                  . α6       .          β5 .       α7  .      .
CD11a     KHFQTKESQETLHKFASKPASEFVKILDTFEKLKDLFTELQKKIYVIE
vWF-A1          ··19aa··              AFVLSSVDELEQQRDEIVSYLCDLA
vWF-A2          ··16aa··              PILIQDFETLPREAPDLVLQRCC
FSA       6406688015202400195275002205406306401551266279 8
```

FIG. 2. Sequence alignment of the CD11a I-domain and vWF A domains. The amino acid sequence of the CD11a I-domain is shown with residues involved in coordinating the manganese colored purple and exposed hydrophobic residues near the manganese-binding site colored green. The secondary-structure assignments obtained by using the algorithm of Kabsch and Sander (27) as implemented in PROCHECK (28) are indicated. Sites of type 2b vWD-causing mutations in the vWF A1 domain are colored red, whereas sites of type 2a vWD-causing mutations in the vWF A2 domain are colored blue. Fractional solvent accessibility (FSA) is shown in green for each residue in the CD11a structure. The FSA is the ratio of the solvent-accessible surface area of a residue in a Gly-Xaa-Gly tripeptide vs. that in the CD11a I-domain structure. A value of 0 represents a value from 0.00 to 0.09, 1 represents 0.10 to 0.19, and so on.

region does not lead to aggregation of this domain as judged by dynamic light scattering, however, and this domain is soluble to at least 15 mg/ml in aqueous solution.

The exposed hydrophobic ridge provides a plausible binding site for the ICAMs. Considerable free energy could be gained by burying these residues at an appropriate intermolecular interface, and several hydrophobic residues in ICAM-1 and ICAM-3 exist in positions likely to be solvent exposed and near residues that affect the CD11a/CD18–ICAM interaction when mutated (e.g., residues 44–46 and 66 in ICAM-3 and residues 42–44 and 64 in ICAM-1) (29). The proximity of this hydrophobic ridge to the metal-binding site makes involvement of these residues in ligand binding consistent with speculation that an exposed coordination site on the metal ion may coordinate an acidic side chain from a ligand molecule (17). Only one position in the exposed hydrophobic ridge identified in CD11a remains hydrophobic for both CD11b and CD11c, suggesting that a high degree of hydrophobicity in this region is not a general requirement for I-domain activation and may be specific to the interactions of CD11a. The probable presence of I-domain-like structures in integrin β subunits (17), however, indicates that structural rearrangements in I-domain-like structures may prove a general feature of affinity modulation by integrins.

The homology between the CD11a I-domain and A-type domains from vWF allows mapping of the position of vWD causing mutations in the A1 and A2 domain of vWF onto the CD11a I-domain structure. vWD is an hereditary bleeding disorder of man that results from abnormalities of vWF (16). An alignment of CD11a and vWF amino acid sequences is shown in Fig. 2. By using the fractional solvent accessibility of the amino acids in CD11a structure as a guide, the hydrophobic β-strands of these domains could be confidently aligned. Gaps in the sequence alignment were left in less certain regions. All but two of the type 2b vWD-causing mutations catalogued in ref. 30 are shown in red in Fig. 4 and can be seen to cluster in a single area of the molecule. The two mutations not shown could not be confidently placed in the CD11a sequence, but it is likely that they map to this area also. The majority of these mutations occur at solvent-exposed sites (Fig. 4). The affinity of vWF for its platelet receptor, GPIb, is normally not observable, and an activation event is required for a high-affinity interaction. Mutations causing type 2b vWD result in a gain-of-function phenotype in which vWF has a constantly high affinity for GPIb. Mutations at several positions of a ligand–receptor binding site are more likely to decrease the affinity of the interaction than increase it as is seen in type 2b vWD, and mutations of solvent-exposed residues are unlikely to alter the global structure of the molecule. We therefore speculate that the vWF A1 mutations cause type 2b vWD by interfering with an interaction of vWF A1 domains that normally inhibits GPIb binding (either sterically or by inducing an inactive conformation) and that the site of these mutations does not represent the GPIb-binding site. A scanning mutagenesis study of vWF led to a similar conclusion (31).

Sites of type 2a vWD-causing mutations in the vWF A2 domain are shown in blue in Fig. 4. The sites of these mutations

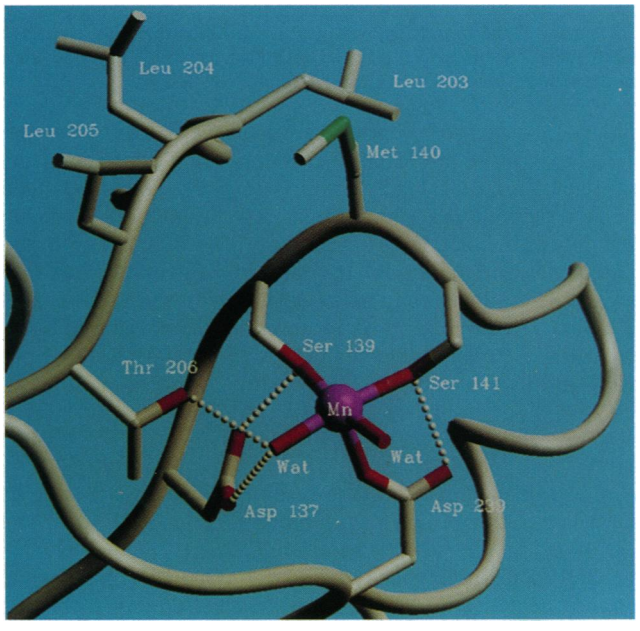

FIG. 3. Diagram of the manganese coordination site. Solvent-exposed hydrophobic residues near the manganese-binding site are shown along with the residues and two waters involved in coordinating the manganese ion. Dots indicate hydrogen bonds. Not shown is a chloride ion that occupies the sixth manganese coordination site. This figure was made with the program SETOR (31).

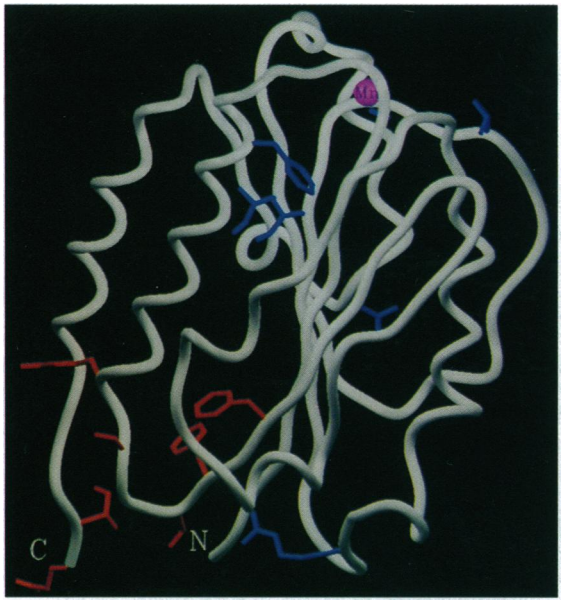

FIG. 4. Sites of vWD-causing mutations. A representation of the CD11a I-domain backbone is shown in white with the manganese shown in purple. Side chains of sites of type 2a vWD-causing mutations are shown in blue and sites of type 2b vWD-causing mutations are shown in red. The mutation sites are identified in Fig. 2. The side chains shown are those of CD11a. This figure was made with the program SETOR (31).

are not localized and seem to reflect the multiple molecular mechanisms that can give rise to the type 2a vWD phenotype. In general, mutations at exposed or hydrophilic sites result in enhanced proteolysis of vWF in plasma, whereas mutations at hydrophobic sites result in impaired biosynthesis of vWF (30). Not all type 2a mutations fit this pattern, but identifying the structural location of future vWD mutations may nonetheless prove a useful tool when classifying vWD subtypes and considering possible molecular mechanisms of various forms of vWD.

We thank James Hildreth and Margaret Guo for providing us with THP-1 cells; Traci Hall, Steve Soisson, Craig Ogata, and the staff at X-4A for assistance during synchrotron data collection; J. Evan Sadler for discussions concerning vWF mutations; Tom Terwilliger for providing the program HEAVY; and Gene Marcantonio and our colleagues at Johns Hopkins University for critical comments on the manuscript. Beamline X4A at the National Synchrotron Light Source is supported by the Howard Hughes Medical Institute. This research was supported by Grant HL51202 from the National Institutes of Health, a Searle Scholar award, and a Junior Faculty Research Award from the American Cancer Society to D.J.L.

1. Hynes, R. O. (1992) *Cell* **69,** 11–25.
2. Harvey, J. E., Hogg, N. & Landis, R. C. (1993) in *Lymphocyte Adhesion Molecules*, ed. Shimizu, Y. (Landes, Austin, TX), pp. 26–54.
3. Larson, R. S., Corbi, A. L., Berman, L. & Springer, T. A. (1989) *J. Cell Biol.* **120,** 703–712.
4. Colombatti, A. & Bonaldo, P. (1991) *Blood* **77,** 2305–2325.
5. Diamond, M. S., Garcia-Aguilar, J., Bickford, J. K., Corbi, A. L. & Springer, T. A. (1993) *J. Cell Biol.* **120,** 1031–1043.
6. Michishita, M., Videm, V. & Arnaout, M. A. (1993) *Cell* **72,** 857–867.
7. Landis, R. C., McDowall, A., Holness, C. L. L., Littler, A. J., Simmons, D. L. & Hogg, N. (1994) *J. Cell Biol.* **126,** 529–537.
8. Randi, A. M. & Hogg, N. (1994) *J. Biol. Chem.* **269,** 12395–12398.
9. Bilsland, C. A. G., Diamond, M. S. & Springer, T. A. (1994) *J. Immunol.* **152,** 4582–4589.
10. Kamata, T. & Takada, Y. (1994) *J. Biol. Chem.* **269,** 26006–26010.
11. Kern, A., Briesewitz, R., Bank, I. & Marcantonio, E. E. (1994) *J. Biol. Chem.* **269,** 22811–22816.
12. Dustin, M. L. & Springer, T. A. (1989) *Nature (London)* **341,** 619–624.
13. van Kooyk, Y., van de Wiel-van Kemenade, P., Weder, P., Kuijpers, T. W. & Figdor, C. G. (1989) *Nature (London)* **342,** 811–813.
14. Landis, R. C., Bennett, R. I. & Hogg, N. (1993) *J. Cell Biol.* **120,** 1519–1527.
15. Dransfield, I., Cabanas, C., Craig, A. & Hogg, N. (1992) *J. Cell Biol.* **116,** 219–226.
16. Sadler, J. E. (1991) *J. Biol. Chem.* **266,** 22777–22780.
17. Lee, J., Rieu, P., Arnaout, M. A. & Liddington, R. (1995) *Cell* **80,** 631–638.
18. Tsuchiya, S., Yamabe, M., Yamaguchi, Y., Konno, T. & Tada, K. (1980) *Int. J. Cancer* **26,** 171–176.
19. Studier, F. W., Rosenberg, A. H., Junn, J. & Dubendorff, J. W. (1990) *Methods Enzymol.* **185,** 60–89.
20. Leahy, D. J., Erickson, H. P., Aukhil, I., Joshi, P. & Hendrickson, W. A. (1994) *Proteins Struct. Funct. Genet.* **19,** 48–54.
21. Otwinowski, Z. (1993) in *Proceeding of the CCP4 Study Weekend: Data Collection and Processing,* eds. Sawyer, L., Isaacs, N. & Bailey, S. (Science and Engineering Research Council, Daresbury Lab., Warrington, U.K.), pp. 56–62.
22. Hendrickson, W. A. (1991) *Science* **254,** 51–58.
23. *CCP4: A Suite of Programs for Protein Crystallography*, Science and Engineering Research Council (SERC) Collaborative Computing Project no. 4 (SERC Daresbury Lab., Warrington, U.K.).
24. Jones, T. A. & Kjeldgaard, M. (1991) *Acta Crystallogr.* **A47,** 110–119.
25. Brunger, A. T. (1992) X-PLOR: *A System for X-ray Crystallography and NMR* (Yale Univ. Press, New Haven, CT), Version 3.1.
26. Kraulis, P. J. (1991) *J. Appl. Crystallogr.* **24,** 946–950.
27. Kabsch, W. & Sander, C. (1983) *Biopolymers* **22,** 1–17.
28. Laskowski, R. A., MacArthur, M. W., Moss, D. S. & Thornton, J. M. (1993) *J. Appl. Crystallogr.* **26,** 283–291.
29. Andersen, R. D., Apgar, P. A., Burnett, R. M., Darling, G. D., Lequesne, M. E., Mayhew, S. G. & Ludwig, M. L. (1972) *Proc. Natl. Acad. Sci. USA* **69,** 3189–3191.
30. Rossman, M. G., Moras, D. & Olsen, K. W. (1974) *Nature (London)* **250,** 194–199.
31. Evans, S. E. (1993) *J. Mol. Graphics* **11,** 134–138.
32. Holness, C. L., Bates, P. A., Littler, A. J., Buckley, C. D., McDowall, A., Bossy, D., Hogg, N. & Simmons, D. L. (1995) *J. Biol. Chem.* **270,** 877–884.
33. Ginsburg, D. & Sadler, J. E. (1993) *Thromb. Haemostasis* **69,** 177–184.
34. Matsushita, T. & Sadler, J. E. (1995) *J. Biol. Chem.* **270,** 13406–13414.